Dynamic evolution of a fault system through interactions between fault segments

Ryosuke Ando
Earthquake Research Institute, University of Tokyo, Tokyo, Japan

Taku Tada
Department of Architecture, Faculty of Engineering, Tokyo University of Science, Tokyo, Japan

Teruo Yamashita
Earthquake Research Institute, University of Tokyo, Tokyo, Japan

Received 1 July 2003; revised 1 March 2004; accepted 1 April 2004; published 18 May 2004.

[1] We simulate the dynamic evolution process of fault system geometry considering interactions between fault segments. We calculate rupture propagation using an elastodynamic boundary integral equation method (BIEM) in which the trajectory of a fault tip is dynamically self-chosen. We consider a system of two noncoplanar fault segments: a preexisting main fault segment (fault 1) and a subsidiary one (fault 2) and, allowing the tip of fault 2 to deviate from its original plane, trace its trajectory in the step over region between the two fault segments. Our simulation results show that the final geometry of fault 2 depends on the initial configuration of the two fault segments. If the initial overlap of the two fault segments is smaller than the half length of fault 1, fault 2 coalesces with fault 1 when the step over is narrower than about 1/4–1/2 the length of the latter but is repelled from fault 1 when the step over width is larger than this threshold value. We also show that the inclination angle of fault 2 is sensitive to the rupture velocity; the inclination is larger for faster rupture propagation. Our simulation results imply that as ruptures occur repeatedly, a fault system evolves from an array of relatively small fault segments into a sequence of larger ones. Our results seem consistent with the field observations of natural fault system geometries, which are often characterized by a set of noncoplanar segments interconnected with relatively small jogs at oblique angles. *INDEX TERMS:* 3220 Mathematical Geophysics: Nonlinear dynamics; 7209 Seismology: Earthquake dynamics and mechanics; 7223 Seismology: Seismic hazard assessment and prediction; 7260 Seismology: Theory and modeling; *KEYWORDS:* rupture dynamics, fault interactions, fault geometry

Citation: Ando, R., T. Tada, and T. Yamashita (2004), Dynamic evolution of a fault system through interactions between fault segments, *J. Geophys. Res.*, *109*, B05303, doi:10.1029/2003JB002665.

1. Introduction

[2] Surface traces of natural fault systems usually show complicated geometry, composed of many fault segments bending, bifurcating or separated by step overs [e.g., *Tchalenko and Berberian*, 1975; *Sibson*, 1986a; *Sieh et al.*, 1993; *Sowers et al.*, 1994]. It has been pointed out in previous studies that such nonplanar geometries of fault systems may affect the dynamic processes of rupture including the nucleation, propagation and termination [*King and Nábelek*, 1985; *Sibson*, 1986b]. However, it remains largely unclear how such geometries come to be formed. We focus on the formation processes of fault bends in the present article. Fault bends, or jogs, connecting noncoplanar fault segments at oblique angles, are often observed in step over regions over a broad range of length scales from 100 m to 10 km [e.g., *Tchalenko and Berberian*, 1975; *Segall and Pollard*, 1983; *Sowers et al.*, 1994]. It is very important for seismic hazard assessment whether any given set of two fault segments coalesce with each other during a rupture episode, because the final geometry of a fault system determines not just the dynamic rupture processes but also the magnitude of the earthquake event.

[3] The 1992 Landers, California, earthquake produced a surface trace that typically exemplifies such complicated fault geometry. The fault system, along which the earthquake occurred, is composed of several major noncoplanar fault segments, e.g., the Johnson Valley fault and the Homestead Valley fault, as well as minor fault segments connecting them in step over regions, e.g., the Kickapoo fault (Figure 1). The rupture is considered to have propagated across all three major segments, transferred from one segment to another [*Wald and Heaton*, 1994], and a numerical simulation study has suggested that the presence of the minor cross segments facilitated the transfer [*Aochi and Fukuyama*, 2002]. It is interesting to note that the minor

0148-0227/04/2003JB002665$09.00

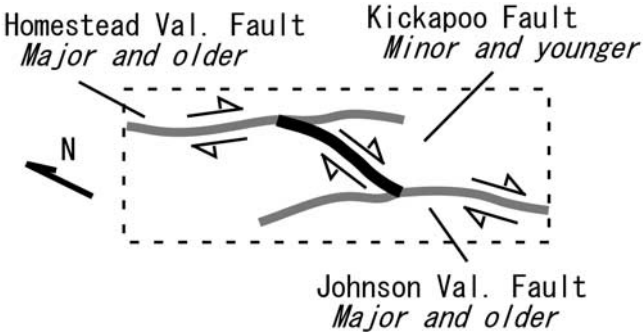

Figure 1. Surface trace of the 1992 Landers, California, earthquake fault; enlarged map of the part where the Johnson Valley, Kickapoo, and the Homestead Valley faults meet [see *Sieh et al.*, 1993].

fault segments are considered younger than the major ones [*Sieh et al.*, 1993; *Sowers et al.*, 1994].

[4] Fractures of relatively small scales are often observed in step over regions lying between macroscopic noncoplanar segments of natural fault systems [e.g., *Segall and Pollard*, 1983; *Granier*, 1985; *Segall and Simpson*, 1986; *Sibson*, 1986a; *Sowers et al.*, 1994]. This suggests that the average fracture strength is lower in such regions than in the surrounding country rock, even though no macroscopic weak plane may be found there. It is thus likely that as shown in Figure 2, the tip of a fault segment extends itself, at some stage during the recurrence of earthquakes, into such a weak step over region with no preexisting weak plane (in the following, we refer to a region with no preexisting macroscopic weak plane simply as an ''intact'' region).

[5] There have been a number of simulation studies on dynamic rupture propagation along faults with nonplanar geometries [*Harris et al.*, 1991; *Harris and Day*, 1993, 1999; *Aochi et al.*, 2000; *Aochi and Fukuyama*, 2002]. However, these studies dealt with the propagation of rupture along predetermined fault planes, and the formation processes of nonplanar fault geometries are still open questions to be answered.

[6] Even though the formation processes of fault systems remain unclear, the important role the interactions between fault segments play in such processes have been pointed out in different simulation studies. A number of authors have quasi-statically simulated pure mode I (in-plane tension) or mixed-mode rupture under a tensile load [e.g., *Olson and Pollard*, 1991; *Renshaw and Pollard*, 1994], and have successfully reproduced the characteristic geometry of fault bends linking noncoplanar fault segments. Recently, *Seelig and Gross* [1999] extended this to a dynamic modeling of mode I rupture and showed that a similar geometry was formed. In both categories of cases, the mechanical fault interactions, mediated by stress perturbations due to the presence of the fault segments, played a crucial role, and noncoplanar fault segments were shown to bend and coalesce with each other. However, earthquake faults are associated with macroscopic shear ruptures caused by a regional shear load under high compressive stress, and the analysis of tensile ruptures cannot be regarded as a sufficiently appropriate model for earthquake ruptures. Simulation studies of mode II (in-plane shear) ruptures under a shear load have been quite rare in number in comparison with tension modeling. To our knowledge, only *Du and Aydin* [1993, 1995] simulated quasi-static mode II rupture, and demonstrated a coalescence of fault segments similar to what was seen in mode I modeling.

[7] Dynamic simulation of the evolution of a mode II shear fault system subject to interactions between different fault segments has not been carried out before because of the mathematical difficulties involved and the limitation of computer resources. However, different studies have pointed out the importance of dynamic effects in rupture propagation processes. In the quasi-static case, and when the rupture velocity is much smaller than the *S* wave speed, the shear traction arising beyond the tip of an isolated fault takes a maximum value in the direction of the original fault plane [*Freund*, 1990; *Kame and Yamashita*, 1999a, 1999b, 2003; *Poliakov et al.*, 2002]. In such cases, an isolated model fault never bends as long as we assume that the fault extends in the direction that maximizes shear traction beyond the tip. On the other hand, as shown by *Kame and Yamashita* [1999a, 1999b], an isolated model fault begins to bend by itself under this maximum shear traction criterion when the rupture velocity becomes close to the *S* wave speed. This fact gives an ample proof that quasi-static modeling is not sufficient to the study of the evolution of fault geometry associated with dynamic ruptures.

[8] The purpose of the present study is to qualitatively investigate the effects of the interactions between fault segments and of dynamic rupture propagation on the evolution of fault system geometries. We have developed a computation algorithm based on an elastodynamic boundary integral equation method (BIEM), capable of dealing with both interactions between fault segments and the effects of dynamic wave propagation. With this BIEM, we allow the fault tip path to be self-chosen; we determine the orientation of fault tip extension by the maximum shear traction criterion mentioned above. First we discuss the basic characteristics of the stress field around an isolated fault. Next we simulate the interactive evolution of a system of two noncoplanar fault segments (for simplicity, we refer to fault segments simply as ''faults'' in the following). We finally present a point of view on the mode of evolution of fault system geometry on the basis of the insights obtained for the isolated fault case.

2. Model

2.1. Method of Numerical Simulation

[9] We employ an elastodynamic and elastostatic boundary integral equation method (BIEM) [e.g., *Tada and*

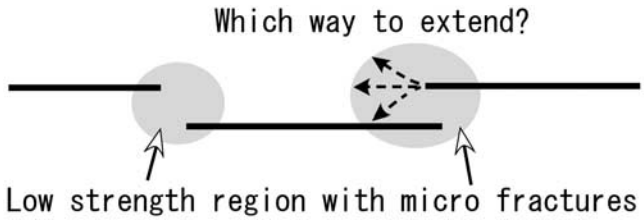

Figure 2. Schematic illustration of the step over regions between fault segments. The shaded parts denote regions of low strength due to the presence of microfractures.

Yamashita, 1997; *Tada and Madariaga*, 2001] for the simulation of rupture propagation in a two-dimensional (2-D) infinite, homogeneous and isotropic medium. We consider mode II ruptures where opening of the fault is prohibited. We discretize the fault plane into an array of linear elements of length Δs and time into a sequence of intervals of duration Δt, and assume that the slip velocity takes a constant value everywhere and at every moment inside any given spatiotemporal discrete element (the assumption of piecewise constant slip velocity). We numerically evaluate the discrete form of the boundary integral equations (BIEs):

$$T^{in} = -\frac{\mu}{2\beta} D^{in} - \frac{\mu}{2\beta} \sum_{\substack{j \\ m \le n-1}} D^{jm} K_{\mathrm{dyn}}^{i,j,n,m} + \frac{\mu}{\pi}(1-p^2) \sum_{j} S^{j} K_{\mathrm{stat}}^{i,j} \quad (1)$$

$$p \equiv \beta/\alpha, \quad (2)$$

where T^{in} is the shear traction at the ith spatial node and nth time step, D^{jm} is the slip velocity at the jth spatial node and mth time step, S^j is the prescribed static slip at the jth spatial node, μ is the shear modulus, α and β are the P and S wave speeds, respectively, and $K_{\mathrm{dyn}}^{i,j,n,m}$ and $K_{\mathrm{stat}}^{i,j}$ are the convolution kernels for the dynamic and static stress fields, respectively (see Appendix A for full expressions). In the present study we consider a Poisson solid and set $p = 1/\sqrt{3}$.

[10] The BIEM has an advantage in the analysis of arbitrarily shaped nonplanar faults, since a nonplanar fault can easily be approximated by an assembly of small planar fault elements. Another advantage of the BIEM is that we do not need to prescribe the geometry of the fault beforehand; the fault tip path can be modeled as dynamically self-chosen as time advances. These advantages suit the purposes of our present study. BIEs generally have hypersingularities at the source point, as well as along the wave fronts in the dynamic case, and they pose difficulties in the numerical evaluation of integrals. However, the hypersingularities have been removed by the technique of integration by parts [*Cochard and Madariaga*, 1994; *Tada and Yamashita*, 1997] in the BIEs we use in the present study.

[11] We introduce an artificial damping term in the numerical scheme in order to suppress short-wavelength oscillations that tend to appear in the slip velocity profile as model time proceeds [*Yamashita and Fukuyama*, 1996]. After we have calculated the slip velocity profile D^{in} along the faults at each time step n, we smooth it spatially by

$$D_{\mathrm{damp}}^{in} = D^{in} + c\left(D_{\mathrm{damp}}^{i-1,n} + D_{\mathrm{damp}}^{i+1,n} - 2D_{\mathrm{damp}}^{in}\right). \quad (3)$$

In the present paper, we set c at 0.5, the same value used by *Yamashita and Fukuyama* [1996].

2.2. Criterion for Fault Tip Extension

[12] We employ the hoop shear maximization criterion [*Koller et al.*, 1992; *Kame and Yamashita*, 1999a, 1999b] to determine the angle of fault tip extension. The hoop shear $\tau_t(\varphi)$ is defined as the magnitude of shear traction on the plane emanating from the fault tip at a given inclination angle φ (Figure 3), which is measured counterclockwise from the original fault plane. We evaluate the hoop shear $\Delta s/2$ ahead of the fault tip, i.e., the midpoint of the fault element to be broken next. At each time step, we evaluate $\tau_t(\varphi)$ at 1 deg intervals over the whole range of φ that does not deviate more than $\pm 90°$ from the orientation of the fault tip extension that occurred last, and we search for the angle $\varphi_{\max}$ that maximizes $\tau_t(\varphi)$. The fault tip is made to advance by one element in the direction $\varphi_{\max}$ at a prescribed time step so that the rupture velocity v_r is kept constant at a prescribed value. We assume no shear friction on the ruptured part of the fault and consider no slip-weakening process; the shear traction is totally released at the fault tip at the very moment when it is broken. Bifurcation of the fault tip is not considered.

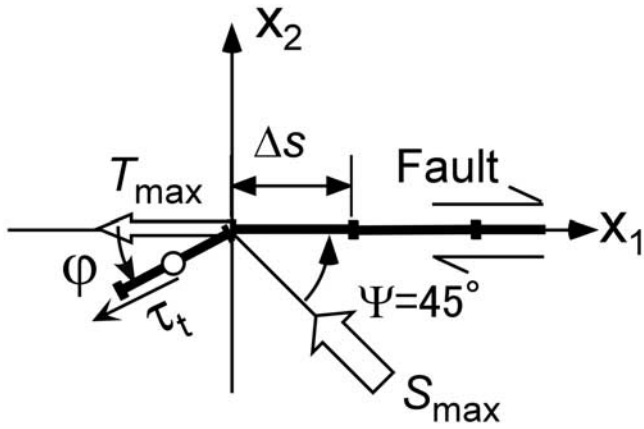

Figure 3. Definition of the hoop shear traction. The hoop shear $\tau_t(\varphi)$ is evaluated at the point denoted by an open circle, located $\Delta s/2$ ahead of the fault tip, and the fault tip is assumed to extend in the direction that maximizes $\tau_t(\varphi)$. The initial fault plane, which is parallel to the axis of maximum principal stress $T_{\max}$, is inclined at an angle of $\Psi = 45°$ to the axis of maximum principal stress $S_{\max}$.

[13] We do not take account of the effects of normal stress on the orientation of fault tip extension. In fact, the Coulomb friction law, which states that the shear frictional strength varies linearly with the normal stress, is a strictly empirical law known for the macroscopic behavior of a preexisting weak plane under quasi-static loading [*Scholz*, 2002, section 1.1.5], and it remains unclear what effects the normal stress has on the local behavior of a fault tip where intact rock is being dynamically fractured. Some authors have incorporated the effects of normal stress in the fracture criterion in their simulation studies [e.g., *Harris and Day*, 1993; *Kame et al.*, 2003], but it should be borne in mind that their approach was valid in so far as they dealt with rupture propagation along preexisting weak planes. In most part of the present study, we also do not consider the effect of regional stress, applied at infinity, on the orientation of fault extension, because the aim of this paper lies in evaluating the effects of fault interactions qualitatively and in isolating them from other effects. The effects of the regional and normal stresses will be further discussed in section 4.5, and discussion continues in section 5 with respect to the relative scaling of tensile microcracks in laboratory experiments.

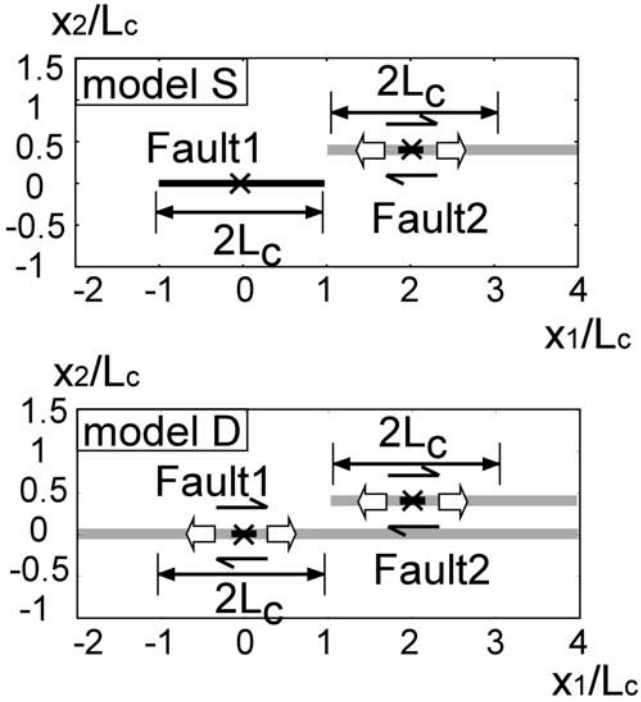

Figure 4. Initial geometry of our model faults. Thick and gray lines denote prescribed weak planes.

[14] As shown in a later section, the angular variation profile of the hoop shear traction is sensitive to the rupture velocity v_r. In the present study, we keep v_r constant throughout each numerical run, in order to eliminate the influences the variations in v_r can have on the trajectory of the fault tip.

2.3. Model of Interacting Faults

[15] We consider a set of two noncoplanar faults lying in an infinite 2-D elastic medium on which a uniform regional load is applied at infinity, since such a simple fault configuration can be regarded as a prototype for more complicated systems consisting of three or more faults. The two faults are initially oriented at an angle of $\Psi = 45°$ counterclockwise from the axis of maximum principal stress S_{max} (Figure 3), i.e., the orientation of maximum shear T_{max} when the regional stress field alone is considered. Under this assumption, for a given inclination angle φ measured counterclockwise from the fault plane, the amount of shear traction drop expected on a fault oriented at that angle is $\Delta\sigma(\varphi) = \sigma_{max}\cos 2\varphi$, which means that negative traction drop is expected to occur outside the range $-45° < \varphi < 45°$. We also examine the cases of $\Psi = 35°$ and $55°$ in section 4.5 where we discuss the effects of regional stress.

[16] We consider a preexisting main fault (fault 1) and a subsidiary one (fault 2) that is formed along a prescribed weak plane off the plane of fault 1 (Figure 4). We fix the origin of the x_1x_2 coordinate system at the midpoint of fault 1 and define the x_1 axis along the plane of fault 1. For the sake of simplicity, fault 2 is nucleated at a prescribed location, is propagated bilaterally, and is allowed to bend at its left tip when the length of fault 2 has reached 22 discrete elements. In physical terms, this bending condition corresponds to the situation in which the fault tip has outgrown the end of a preexisting weak plane and begins to extend itself into an intact region.

[17] We consider two models, model S and model D (Figure 4), with different assumptions concerning fault 1. In model S, we prescribe a static slip on fault 1 corresponding to a homogeneous shear traction drop of $\Delta\sigma$ and a fault length of $L = 22\Delta s$ and assume that fault 1 does not break during the dynamic propagation of fault 2. In model D, on the other hand, fault 1 is nucleated at a point simultaneously with the nucleation of fault 2, and is propagated bilaterally along the prescribed weak plane at the same fixed speed v_r with fault 2. In physical terms, model S corresponds to the case where fault 1 has already been ruptured in the past, and deals with the interactions between a stationary main fault and a dynamically propagating subsidiary fault. Model D deals with the dynamic interactions between two faults nucleated simultaneously.

[18] Model D deals with an idealized case, and we do not necessarily believe that situations precisely like in model D can actually be found out in nature; it is simply in order to isolate the effects of fault interactions from other factors and to reduce the number of model parameters that we made the somewhat unrealistic assumption that rupture starts simultaneously on the two faults in model D. In addition, dynamic jumping of rupture fronts, sometimes observed in spontaneous rupture models, can lead to a case where model D is applicable.

[19] In our modeling, the length of fault 1 is fixed at $22\Delta s$ in model S, while in model D, fault 2 begins to bend when fault 1 has grown that long. We denote this characteristic length by $2L_c = 22\Delta s$, as it is an important parameter which scales the profile of the stress field around the fault system. In the following, we show our simulation results with all spatial length scales normalized by L_c.

3. Stress Field Around an Isolated Planar Fault

[20] In this section, we discuss basic characteristics of the static and dynamic stress field around an isolated planar fault in an infinite medium. Since fault interactions are mediated by the stress field perturbations by the presence of faults, knowledge of the case of an isolated fault gives a clue to understand the behavior of more than one interacting faults.

3.1. Static Stress Field Around an Isolated Planar Fault

[21] We first consider the static stress field around an isolated planar fault with a homogeneous shear traction drop $\Delta\sigma$ over its entire length. The x_1x_2 coordinate system is defined in the same way as for fault 1 in the above mentioned model of two interacting faults. We computed the stress distribution using the known analytic solutions to this problem (Appendix B) [e.g., *Pollard and Segall*, 1987]. The direction θ_{max} of maximum shear traction, measured counterclockwise from the positive x_1 axis, is given, using the stress components, by

$$\tan(2\theta_{max}) = -\frac{1}{2}\frac{\sigma_{11} - \sigma_{22}}{\sigma_{12}}. \quad (4)$$

Figure 5 shows the orientation and magnitude of the maximum static shear traction $\Delta\tau_{max}$ around an isolated

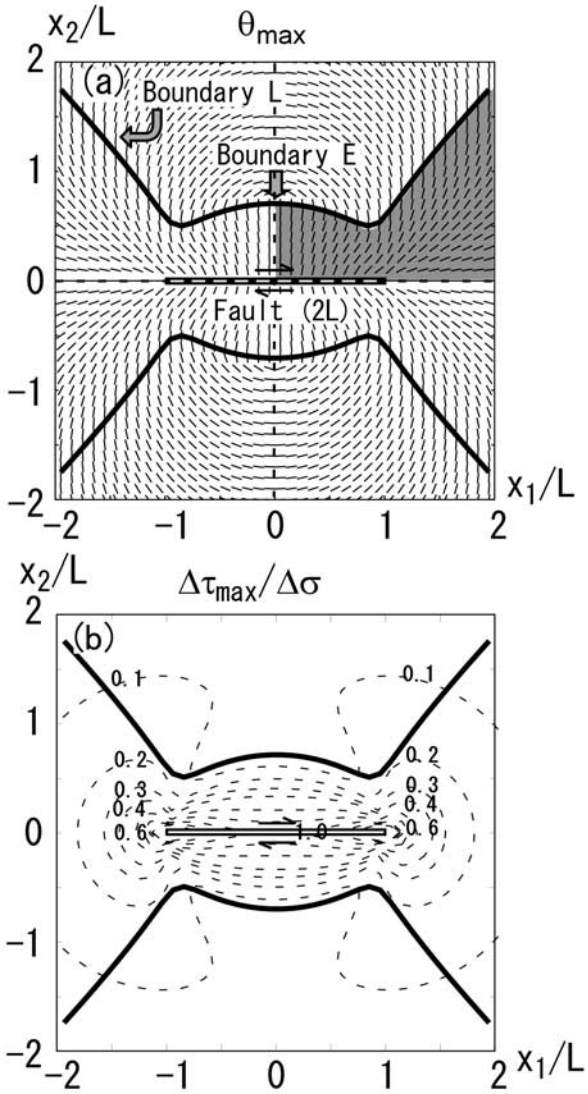

Figure 5. (a) Spatial distribution of the orientation of maximum static shear $\Delta\tau_{max}$ (shown with small line segments) around an isolated fault with a homogeneous shear traction drop $\Delta\sigma$. (b) Contour map of the magnitude of $\Delta\tau_{max}$ normalized by $\Delta\sigma$. Solid curves denote boundaries across which the orientation of maximum shear switches inclinations (boundaries E and L).

fault. As is naturally expected, the orientation of maximum shear is distributed symmetrically with regard to two axes of symmetry, namely the fault plane and its perpendicular bisector. The solid curves in Figures 5a and 5b represent boundaries across which the orientation θ_{max} of maximum shear switches inclinations; on the boundaries, $\theta_{max} = \pm 90°$, and from equation (4), the identity

$$\sigma_{11} - \sigma_{22} = 0 \tag{5}$$

holds there. In the first quadrant in Figure 5a, for example, the inclination θ_{max} falls in the range $0° < \theta_{max} < 90°$ on the lower side of the boundary, whereas $-90° < \theta_{max} < 0°$ on the upper side of it.

[22] These boundaries are made up of elliptic-shaped parts lying close to the center of the fault and linear-shaped parts extending from there to infinite distance. In the following, we refer to the former as boundary E and to the latter as boundary L. As shown in Figure 6, the shape of boundary E is roughly approximated by the elliptical curve $(x_1/1.1)^2 + (x_2/0.7)^2 = 1$, while boundary L converges to the asymptote $x_1 = x_2$.

3.2. Dynamic Stress Field Around an Isolated Planar Fault

[23] We next consider the dynamic stress field around an isolated self-similar planar fault that is propagated bilaterally at a constant rupture velocity with a homogeneous shear traction drop. Analytic solutions are known for the stress field around such a self-similar fault [*Kostrov*, 1964; *Kikuchi*, 1976; *Tada*, 1995] (Appendix B).

[24] Figure 7 shows the orientation and magnitude of the maximum shear traction around a self-similar fault propagating at 0.9 times the *S* wave speed. Comparison of Figures 5 and 7 reveals that the dynamic traction profile possesses qualitatively the same features as its static counterpart, though the shape of the boundaries $\theta_{max} = \pm 90°$ (solid curves) is somewhat different: boundary E has a smaller radius of curvature and the joints between boundaries E and L lie closer to the fault tips in the dynamic case. Also, the magnitude of $\Delta\tau_{max}$ on those boundaries is somewhat larger in the dynamic case.

[25] Figure 7a, 7c, and 7d show the dependence of the shape of these boundaries on the rupture velocity v_r. We can recognize a gradual change in the shape of the boundaries as v_r varies. We have found that the magnitude of $\Delta\tau_{max}$ on the boundaries becomes larger as v_r increases.

3.3. Effect of a Rapidly Propagating Fault Tip on the Hoop Shear Traction

[26] Finally, we discuss the angular variation profile of the hoop shear traction in the neighborhood of a fault tip that is propagated at a high constant rupture velocity v_r. Figure 8 shows the v_r dependence of the hoop shear

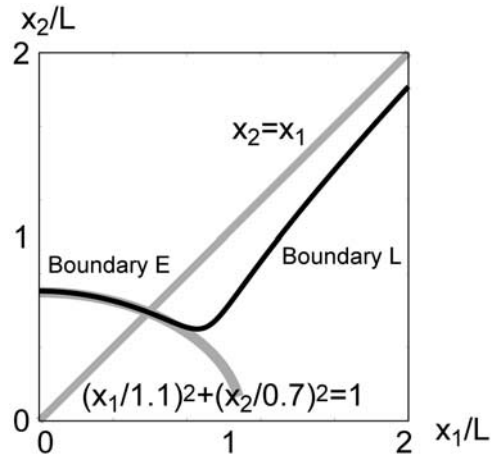

Figure 6. Geometry of boundaries E and L (black curves). Boundary E can be roughly approximated with an elliptical curve (shown in gray), and boundary L has an asymptotic line (shown in gray).

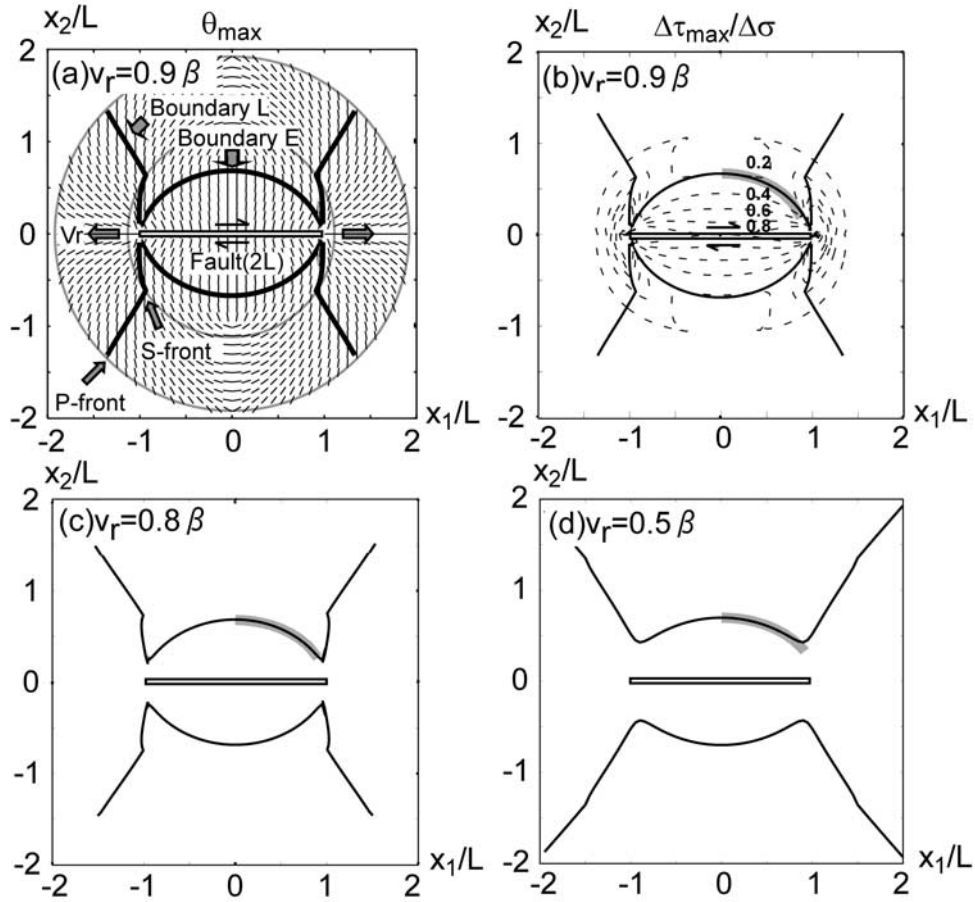

Figure 7. (a) Spatial distribution of the orientation of maximum dynamic shear $\Delta\tau_{max}$ around an isolated self-similar fault with a homogeneous shear traction drop $\Delta\sigma$ and a rupture propagation velocity of $v_r = 0.9\beta$. (b) Contour map of the magnitude of $\Delta\tau_{max}$, normalized by $\Delta\sigma$, for $v_r = 0.9\beta$. The shape of boundaries E and L is also shown. (c) and (d) Shape of boundaries E and L for the cases of $v_r = 0.8\beta$ and 0.5β, respectively. The elliptical curve that approximates boundary E is given, in each case, by the equations $(x_1/0.92)^2 + (x_2/0.68)^2 = 1$ (Figure 7b), $(x_1/0.98)^2 + (x_2/0.68)^2 = 1$ (Figure 7c), and $(x_1/1.04)^2 + (x_2/0.70)^2 = 1$ (Figure 7d).

profile. The traction begins to show an ''m''-shaped angular profile and the axis of maximum shear deviates from the original fault plane when v_r exceeds a critical value $v_c \approx 0.77\beta$, as has been pointed out by other authors [*Freund*, 1990; *Kame and Yamashita*, 1999a, 1999b; *Poliakov et al.*, 2002]. This ''m''-shaped profile is peculiar to the dynamic model and does not occur in the quasi-static case; *Kame and Yamashita* [1999a, 1999b] showed, for example, that a rapidly propagating fault can begin to bend spontaneously because of the deviation of the maximum hoop shear axis.

[27] The symmetrical shape of the shear traction profile is characteristic of the model of an isolated fault; we show in a later section how the symmetry is broken when more than one faults interact with each other.

4. Simulation of the Evolution of Fault Geometry Through Fault Interactions

[28] In this section, we numerically simulate how the geometry of a system of two faults evolves under mechanical interactions. We demonstrate, in section 4.1 through 4.3, the final geometry of the fault system as well as its dependence on the initial configuration and the rupture velocity. In section 4.4, we present an interpretation of the mode of evolution of fault system geometry in terms of the

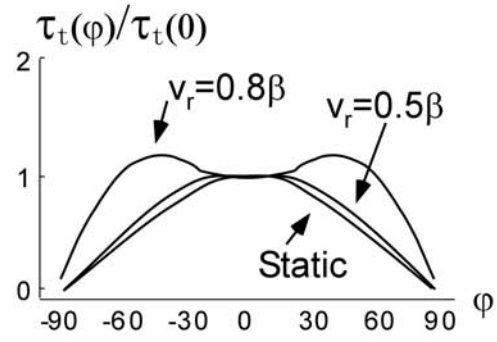

Figure 8. Angular variation profiles of the hoop shear traction at the fault tip: the three curves correspond to the rupture propagation velocities of $v_r = 0.8\beta$ and 0.5β and to the static fault case.

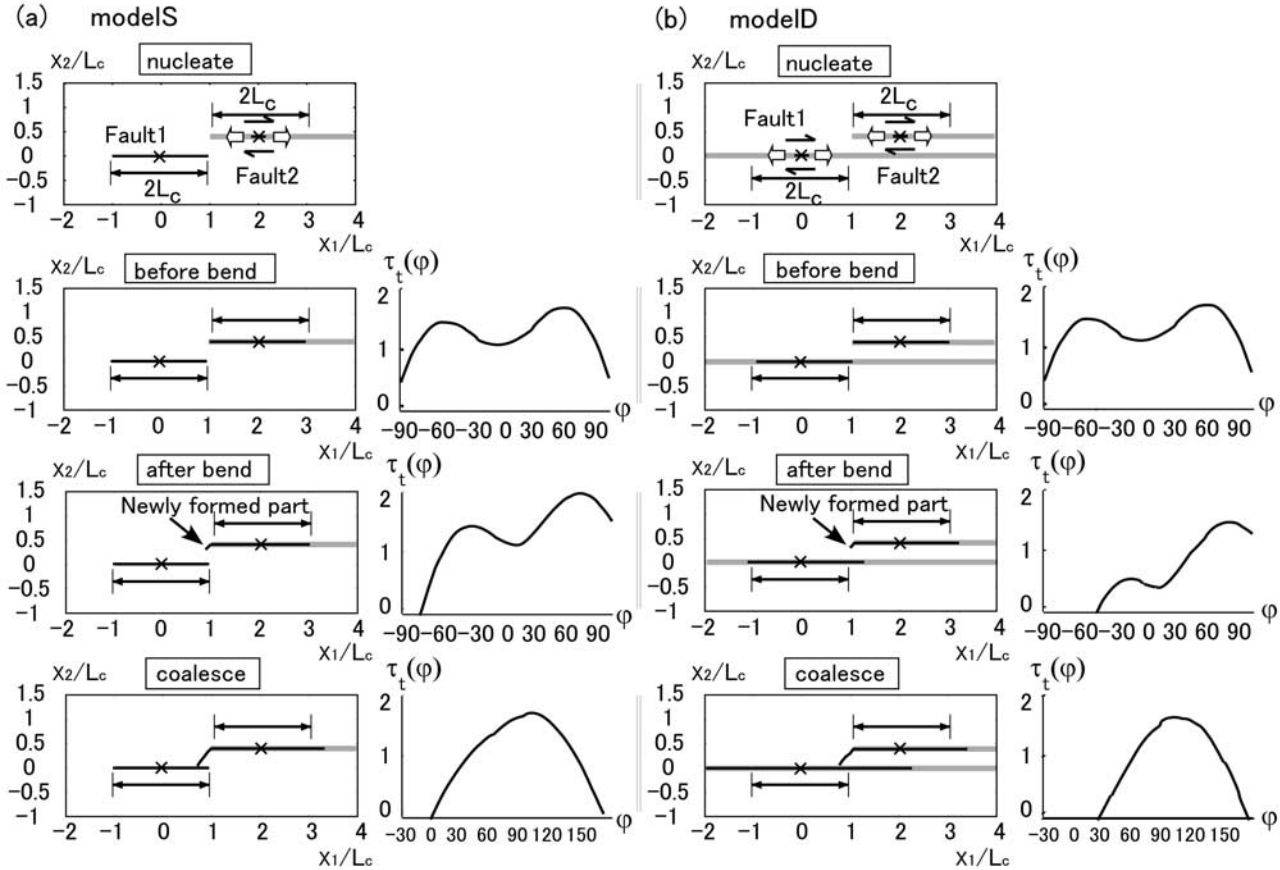

Figure 9. Snapshots of fault evolution in (a) model S and (b) model D. The angular variation profile of the hoop shear traction at the left tip of fault 2 is given on the right of each panel. The gray lines denote the preexisting weak planes, while crosses mark the nucleation points of the two faults; in model S, a cross is drawn at the midpoint of fault 1 which is the origin of coordinates. The fault tips were made to propagate at a fixed speed of $v_r = 0.8\beta$.

insights obtained in the previous section for the stress distribution around an isolated fault.

4.1. Evolution of the Fault Geometry in the Step Over Region

[29] The left columns of Figures 9a and 9b show some snapshots of fault geometry for models S and D, respectively, with a fixed rupture velocity of $v_r = 0.8\beta$ prescribed. The right columns show the angular variation profile of hoop shear in the neighborhood of the left tip of fault 2 in each corresponding case. As stated above, the left tip of fault 2 is made to propagate in the orientation φ_{max} of maximum shear after it has entered the intact region; φ_{max} is measured counterclockwise from the negative x_1 axis. Crosses denote locations where faults 1 and 2 are nucleated.

[30] The growth process of fault 2 in the step over region is qualitatively similar for both models S and D. In the examples shown in Figure 9, fault 2 chooses to bend in the direction of fault 1 and finally coalesces with it, because of the asymmetric angular profile of the hoop shear traction beyond the tip of fault 2 caused by the stress perturbation due to the presence of fault 1.

4.2. Dependence on the Initial Configuration

[31] We discuss the dependence of the final geometry of the fault system on the initial fault configuration, which we parameterize with the coordinates (d_1, d_2) of the point where fault 2 begins to bend. d_2 represents the step over width, while $L_c - d_1$ gives the amount of overlap (or underlap) of the two preexisting weak planes measured along strike.

4.2.1. Case of Model S

[32] Figure 10 shows the final geometry of the fault system in model S for four different amounts of fault overlap and for different values of the step over width.

[33] Figures 10a–10c correspond to cases where fault 2 begins to bend before its left tip has traveled beyond the midpoint of fault 1. We recognize a critical value d_2^c for the step over width: fault 2 coalesces with fault 1 when $d_2 < d_2^c$ but is repelled from it when $d_2 > d_2^c$. This critical step over width varies with the fault overlap $L_c - d_1$: d_2^c roughly equals 1.3, 0.5 and 0.7 times L_c for the cases of Figures 10a, 10b, and 10c, respectively.

[34] Figure 10d corresponds to the case where fault 2 begins to bend after its left tip has traveled beyond the midpoint of fault 1. The pattern of coalescence and repulsion is opposite to what we have seen in Figures 10a–10c: repulsion occurs when $d_2 < d_2^c$ and coalescence occurs when $d_2 > d_2^c$, with d_2^c roughly equaling $0.5L_c$.

[35] In all of these cases, slip is found to be occurring even in the parts where the fault inclination is deviated more than 45° from the original plane, but the amount of slip is substantially suppressed. In the modeling of spontaneous

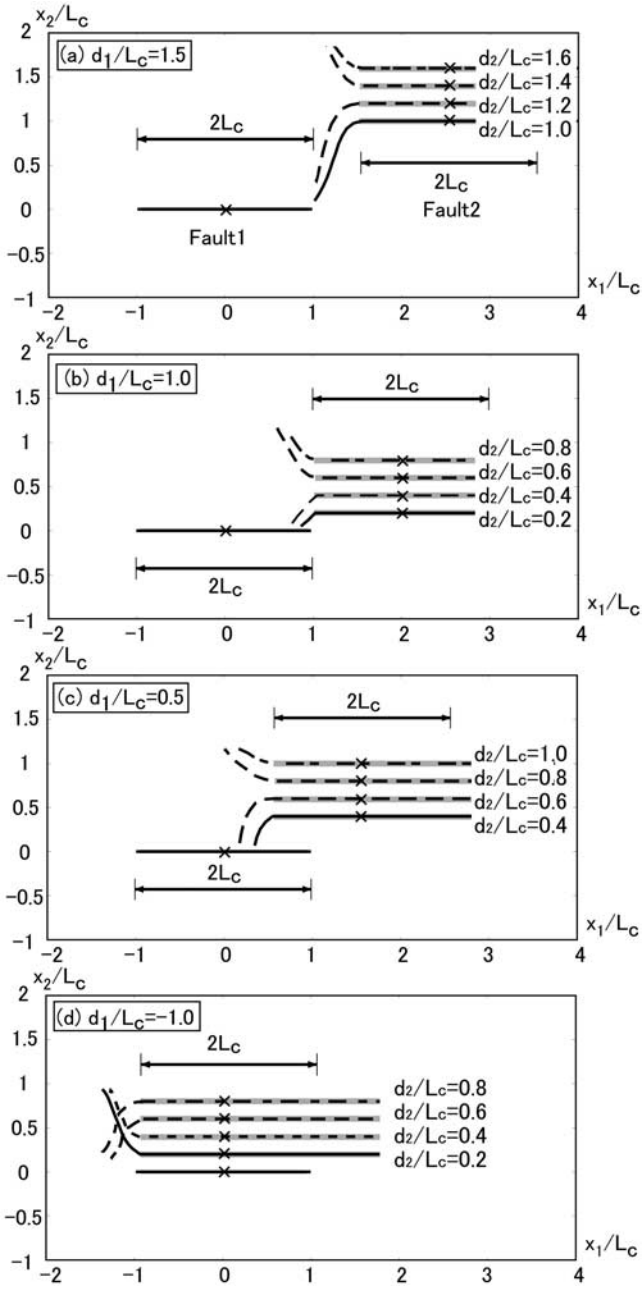

Figure 10. Final fault geometry in model S, for different initial configurations assumed.

rupture propagation under more realistic conditions, fault tip extension tends to be decelerated or arrested in such parts of the fault [*Kame and Yamashita*, 1999a, 1999b].

[36] The dependence of the final geometry of the fault system on the initial configuration can be summarized in the following way, as long as the model cases examined here are concerned: if the overlap of the two weak planes does not exceed half the length of fault 1, (1) fault 2 coalesces with fault 1 when the step over is narrower than about 1/4–1/2 the length of fault 1 ($2L_c$), while (2) fault 2 is repelled from fault 1 when the step over width is larger than this threshold value. If the overlap is larger than half the length of fault 1, (3) fault 2 is repelled from fault 1 when the step over is narrower than about 1/4 to 1/2 the length of fault 1, while (4) fault 2 coalesces with fault 1 when the step over is wider.

4.2.2. Case of Model D

[37] Figure 11 shows the final geometry of the fault system in model D. The initial configuration is again parameterized with (d_1, d_2). Each of the four panels in Figure 11 shows the result for the same amounts of along-strike overlap as in the corresponding panel in Figure 10 (model S).

[38] The pattern of dependence of the final geometry on the initial configuration is qualitatively similar to that in model S. However, the values of d_2^c are slightly different: d_2^c roughly equals 1.3, 0.4, and 0.7 times L_c for the cases of

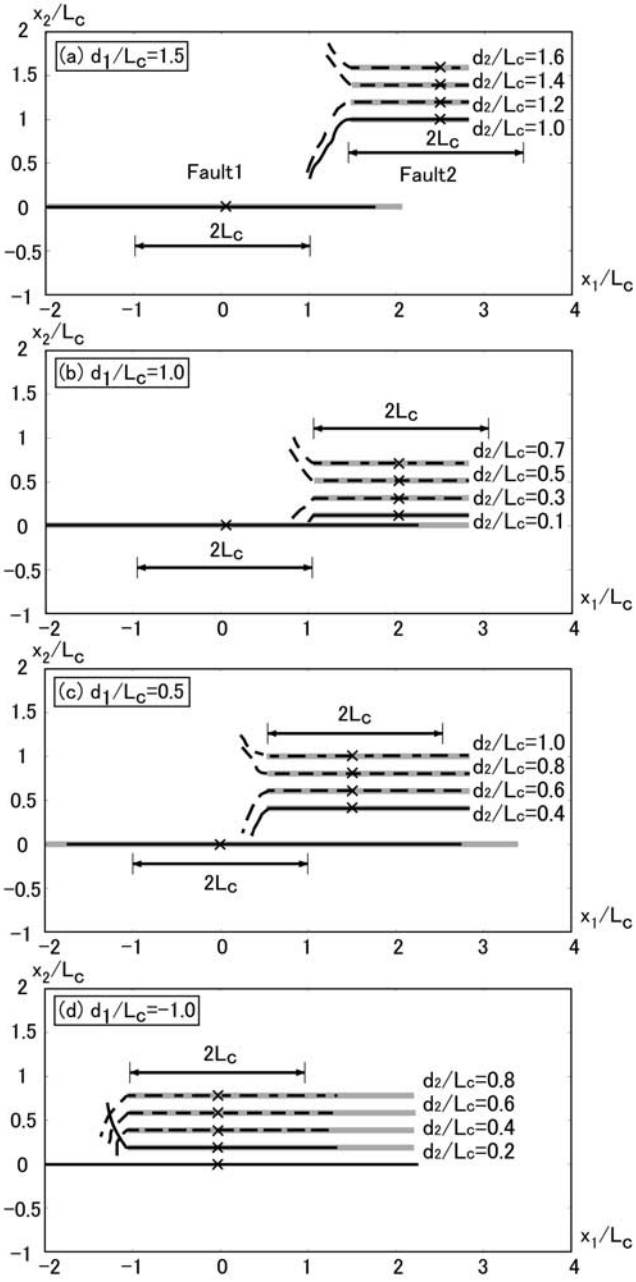

Figure 11. Final fault geometry in model D, for different initial configurations assumed.

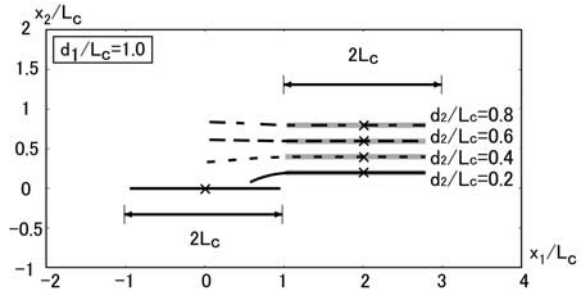

Figure 12. Final fault geometry in model S with fault 2 made to grow quasi-statically.

Figures 11a, 11b, and 11c, respectively, and is marginally smaller than in model S.

[39] We would like to emphasize that the differences in the final geometry of fault 2 in models S and D are due to the intrinsic effects of dynamic versus static stresses and does not directly have to do with quasi-static effects related with different sizes of fault 1, because the length of fault 1 is identical for both models at the very moment when fault 2 starts to bend (second frame from the top in Figure 9). It is true that the two profiles of the hoop shear begin to show visible differences only in the third frame of Figure 9; however, it is the barely visible small differences in hoop shear in the second frame, and not the visible differences in the third frame, that have caused the qualitative difference in the final geometry of the fault system. This interpretation is borne out by the fact that the geometry of the model fault system has never switched patterns between coalescence and repulsion once fault 2 has begun to bend at the time of the second frame (Figures 9–11).

4.3. Dependence on the Rupture Velocity

[40] To investigate the influence of the rupture velocity on the final fault geometry, we conducted numerical simulation with model S while making fault 2 to grow quasi-statically, and compared the result with that of the dynamic case with $v_r = 0.8\beta$ (Figure 10). We employed the elastostatic BIEs of *Tada and Yamashita* [1997] in the quasi-static modeling. We fixed the fault overlap $L_c - d_1$ at $1.0L_c$ as in Figure 10b.

[41] Comparison of Figures 10b and 12 reveals a remarkable difference in the simulation results for the two models: the inclination of fault 2 in the step over region is much steeper in the dynamic than in the quasi-static case. This can be understood in terms of the v_r dependence of the angular distribution of hoop shear (Figure 8): as we have pointed out, the axis of maximum shear deviates from the original fault plane when v_r exceeds a critical value $v_c \approx 0.77\beta$, as does the rupture velocity $v_r = 0.8\beta$ assumed in our dynamic model.

[42] In the quasi-static case, the inclination of fault 2 in the step over region becomes noticeably small with increasing step over width, but we can still see a slight deviation of the left tip of fault 2 from the original fault plane. The pattern of dependence of the final fault geometry, coalescence or repulsion, on the initial configuration is much the same as what we have seen in the dynamic case, and so is the critical value d_2^c for the step over width. On the other hand, the significant decrease in fault tip inclination with increasing step over width can be understood in terms of the decreasing effects of fault interactions, as the static stress perturbation due to the presence of fault 1 is the largest in the vicinity of the tips of fault 1 and rapidly decreases with increasing distance.

[43] We fixed v_r at constant values in our modeling, so that the result may be a little different when spontaneous propagation of rupture with no prescribed velocity is considered. In the latter case, the rupture velocity may begin to decrease with steepening fault tip inclination, as the magnitude of shear traction drop decreases; one is tempted to conjecture that this mechanism of negative feedback may possibly act to prevent the fault from getting inclined too steeply.

4.4. What Determines the Coalescence or Mutual Repulsion of Two Faults?

[44] The incremental stress $\boldsymbol{\sigma}^{\mathrm{incr}}(\mathbf{x}, t)$ at position $\mathbf{x}$ and t due to the occurrence of slip on faults 1 and 2 can be written in a general form as

$$\begin{aligned}\boldsymbol{\sigma}^{\mathrm{incr}}(\mathbf{x},t) = &\int_{\Gamma_1}\int \Delta\dot{u}_1(\xi,\tau)G_{\mathrm{dyn}}(\mathbf{x},t-\tau;\xi,0)d\tau d\xi \\ &+ \int_{\Gamma_1} \Delta u_1(\xi)G_{\mathrm{stat}}(\mathbf{x};\xi)d\xi \\ &+ \int_{\Gamma_2}\int \Delta\dot{u}_2(\xi,\tau)G_{\mathrm{dyn}}(\mathbf{x},t-\tau;\xi,0)d\tau d\xi \\ &+ \int_{\Gamma_2} \Delta u_2(\xi)G_{\mathrm{stat}}(\mathbf{x};\xi)d\xi, \qquad (6)\end{aligned}$$

where ξ is the source location on the fault, τ is the source time, $\Delta\dot{u}_i$ ($i = 1, 2$) and Δu_i are the slip velocity and slip on each fault, respectively, G_{dyn} and G_{stat} are the Green's functions for the dynamic and static stress components of the stress field, respectively, and Γ_i ($i = 1, 2$) is the whole length of each fault. The total stress increment is represented as a superposition of the contributions from slip velocity $\Delta\dot{u}_i$ and slip Δu_i on both faults. For the shear stress components, the first two and the last two terms of the right hand side are symmetrically distributed with regard to the planes of faults 1 and 2, respectively, regardless of the distribution profiles of $\Delta\dot{u}_i$ and Δu_i, as long as the faults are planar: this property can be understood in terms of the symmetry of the Green's functions [*Freund*, 1990; *Tada and Yamashita*, 1997; *Tada and Madariaga*, 2001]. This means that only the first two terms, or the stress perturbation by fault 1, is able to determine which way fault 2 is going to bend when the condition for bending has been satisfied. The direction of fault 2 bending is therefore subject to the orientation of maximum incremental shear due to the presence of fault 1.

[45] We showed in section 4.2 that there is a critical value d_2^c for the step over width across which the orientation of fault 2 bending is switched, and that its value depends on the fault overlap $L_c - d_1$. The meaning of d_2^c becomes much clearer when we associate it with boundaries E and L mentioned earlier. The axis of maximum incremental shear due to fault 1 alone is oriented differently across boundaries E and L relative to the x_1 axis, and this causes fault 2 to bend in opposite directions according to which side of those boundaries the tip of fault 2 happens to fall on. This

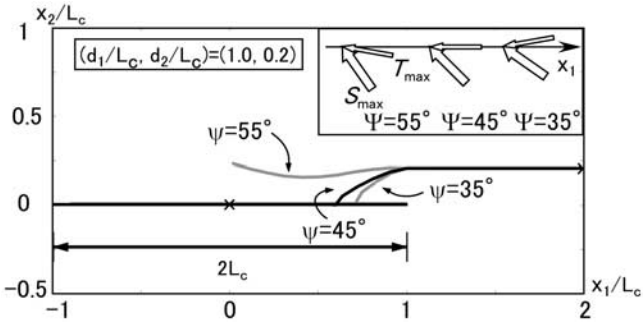

Figure 13. Final fault geometry for model D, for a fixed initial configuration and three different inclinations of the regional stress axis.

explains why, in Figures 10a–10c and 11a–11c, d_2^c takes the smallest value when $L_c - d_1 = 0$ (Figures 10b and 11b): the boundaries come closest to fault 1 at the corresponding location along the x_1 axis.

[46] We have also noted that the pattern of dependence of coalescence or repulsion on the step over width is opposite, in the case of total overlap of the two weak planes (Figures 10d and 11d), to what we have seen when the overlap is smaller than half the length of fault 1 (Figures 10a–10c and 11a–11c). The pattern reversal can also be interpreted in terms of the fact that, across the perpendicular bisector of fault 1, the axis of maximum incremental shear due to fault 1 alone switches orientations relative to the x_1 axis.

[47] We showed that the values of d_2^c are slightly different for models S and D for the same parameter d_1 used. This can be understood by recalling that boundaries E and L take different shapes in the static and dynamic cases (Figures 5 and 7).

[48] *Du and Aydin* [1995] argued, with a modeling of quasi-static mode II faulting, that mutual repulsion of fault tips can occur under the influence of regional stress; they showed that the fault tip tends to extend in the direction of maximum shear due to the regional stress ($\Psi = 45°$ in our notation) when the step over is wider than about half the length of the individual faults and the effects of fault interactions are negligible. They thereby concluded that two noncoplanar faults tend to grow away from each other if the angle Ψ between the initial fault planes and the axis of maximum principal stress is larger than 45° in the case of left steps and smaller than 45° in the case of right steps. Our results imply, however, that two noncoplanar faults can grow to repel each other through mutual interactions alone when the step over is wider than about half the length of the individual faults, even if one does not consider the effects of regional stress. In the present study we used a criterion for determining the orientation of fault tip extension that is slightly different from *Du and Aydin*'s [1995] criterion, but we have confirmed in an earlier study [*Ando and Yamashita*, 2003a] that similar fault configurations result whichever sort of criterion we may use in the numerical modeling.

4.5. Effects of Regional and Normal Stresses

[49] We illustrate how the inclination of regional stress axes may come into play in the evolution of fault geometry; we determine the orientation of fault tip extension by applying the same criterion to the field of total shear traction

$$\tau_t(\mathbf{x}, \Psi, \varphi, t) = \sigma_{\max} \sin(2\Psi + 2\varphi) + \tau^{\text{incr}}(\mathbf{x}, \varphi, t), \qquad (7)$$

where Ψ is the inclination of the initial fault planes measured counterclockwise from the axis of maximum principal stress $S_{\max}$, φ is the orientation of tentative fault tip extension measured counterclockwise from the initial fault planes (Figure 3), and the second term represents the incremental shear traction on the plane of tentative fault extension due to the occurrence of slip on the faults. The first term reduces to $\sigma_{\max} \cos 2\varphi$ when $\Psi = 45°$. Figure 13 shows the final fault geometries for model S, with the initial geometry identical to the case $d_2 = 0.2L_c$ in Figure 10b. For $\Psi = 45°$, the inclination of fault 2 in the step over region is smaller in the presence of regional stress than in its absence. This is because the fault tip tends to be attracted to the orientation of maximum regional shear traction, which is parallel to the initial fault plane in this particular case. For the same reason, fault 1 turns away from fault 2 after momentarily approaching it when $\Psi = 55°$, whereas fault 1 coalesces with fault 2 at a steeper angle than in Figure 10b when $\Psi = 35°$. It should be borne in mind that the fault tip is prone to extend in the direction of maximum regional shear traction, whatever the fault interactions and the effects of higher v_r may be, when the shear traction drop on the fault plane is significantly smaller than $\sigma_{\max}$.

[50] Our model simulation produces strictly symmetric patterns for left-stepping and right-stepping fault system models, but asymmetry is expected when we consider the transfer of rupture onto a preexisting fault as the effects of normal stress come into play. *Harris et al.* [1991] and *Harris and Day* [1993] argued that rupture is more likely to be transferred across a dilational jog (step over) than across a compressional one, because rupture on one fault acts to increase the dilational normal stress on the other in the former case and vice versa (Figure 14). When the models in our present study are concerned, however, the pattern is expected to be reversed once fault 2 coalesces with fault 1 at a sufficiently steep angle; when the jog is

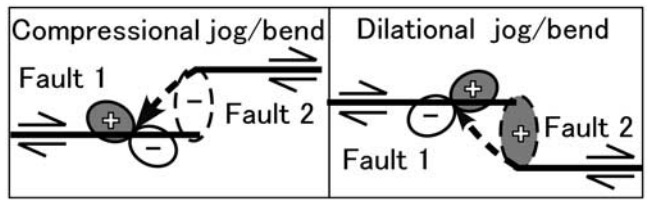

Figure 14. Schematic illustration of a compressional jog and a dilational jog between our two model faults that coalesce. The pluses and minuses denote the increase and decrease, respectively, in volumetric stress caused by the slip on fault 2 and, consequently, the increase and decrease in dilational normal stress on the preexisting fault 1. Dashed circles denote the state of stress perturbation before fault 2 begins to bend, while solid circles denote the state of stress perturbation after fault 2 has coalesced with fault 1.

compressional, rupture on the inclined part of fault 2 tends to increase the dilational normal stress on the part of the preexisting fault 1 that lies ahead, and vice versa. The implication is that rupture is more likely to be transferred across a compressional jog than across a dilational one once coalescence has happened.

5. Implications for Findings From Field Observations and Rock Experiments

[51] Fault bends connecting noncoplanar fault segments at oblique angles are found in a number of surface traces of strike-slip faults observed in the field [e.g., *Tchalenko and Berberian*, 1975; *Segall and Pollard*, 1983; *Sibson*, 1986a; *Sowers et al.*, 1994], and zigzag or sawtooth-shaped geometry can be regarded as a typical feature of natural fault systems. In view of our simulation results, such sort of fault system geometry can be understood as resulting from dynamic interactions between fault segments associated with rupture propagation. In fact, in field observations, the step over between two noncoplanar fault segments connected with a fault jog is narrower than 1/4 to 1/2 the length of individual segments in virtually all reported cases.

[52] The sawtooth-shaped geometries of cracks and faults observed in nature have a typically self-similar structure over a wide range of length scales, from that of fracture surfaces in rock samples [e.g., *Moore and Lockner*, 1995] to that of the San Andreas fault [e.g., *Bilham and Williams*, 1985]. Our simulation results help to understand the origin of this fractality. As we have shown in section 4.2, the final geometry of a fault system formed through dynamic interactions is governed by the characteristic length of its constituent segments. As shown in a number of rock experiments [e.g., *Lockner et al.*, 1992], shear fracture is initiated from an assemblage of numerous microcracks before gradually developing into a macroscopic feature. As a shear fault system grows in size through repeated merger of neighboring cracks or fault segments, the amplitude of its geometrical zigzagging, including the step over widths, increases in proportion to the characteristic length of the constituent segments that play principal roles at the given stage of fault system evolution, resulting in a hierarchical structure of geometrical irregularities which preserve self-similarity over all length scales.

[53] In fracture experiments of intact rock, acoustic emission events generally become localized into a planar zone through successive loading on a sample [e.g., *Lockner et al.*, 1992]. This process can also be understood in terms of our results. Since larger cracks have farther reach of interactive effects, they tend to conjoin larger numbers of cracks than do smaller ones. At the same time, the step over width between two noncoplanar cracks have to be sufficiently small, relative to the individual crack lengths, in order for them to coalesce. This explains why shear rupture tends to be localized into a thin planar zone.

[54] On the basis of fracture experiments of intact rock under high confining pressures, some authors [*Scholz*, 2002; *Moore and Lockner*, 1995; *Lei et al.*, 2000] reported that tensile microcracks form at random locations and in random orientations before planes of localized shear fracture begin to form. We did not take account of such tensile microcracks in our modeling, but they are thought to be much smaller in size than the macroscopic shear cracks we dealt with in the present study, so that we can safely assume that the presence of tensile microcracks do not affect the geometry of the shear fault system. In rock fracture experiments with shear loading, tensile cracks tend to grow large when the confining pressure is low, but shear cracks alone can grow into macroscopic features under high confining pressures [e.g., *Scholz*, 2002]. In the latter case, the size of the tensile cracks is expected to be controlled by the characteristic length scale of the inhomogeneities in the medium, such as the grain size [*Reches and Lockner*, 1994]. In fact, *Moore and Lockner* [1995], who carefully studied the microstructures of rock samples fractured by shear load under high confining pressures, found out no tensile cracks that had grown into scales noticeably larger than the grain size of the specimen.

[55] Our simulation results thus imply that fault systems tend to evolve from an assembly of randomly distributed microcracks, through repeated coalescence of neighboring cracks and fault segments during dynamic rupture in earthquake events, into a large-scale structure of considerable length, such as the San Andreas fault system, capable of causing large earthquakes.

6. Conclusion

[56] We have investigated, with a numerical scheme based on a BIEM, the effects of the interactions between two noncoplanar faults on the resulting fault geometry. Our model consists of a preexisting main fault (fault 1) and a subsidiary one (fault 2) that is formed along a prescribed weak plane off the plane of fault 1, and fault 2 is made to choose by itself the most favorable orientation for fault tip extension after it has outgrown a prescribed length of the preexisting weak plane.

[57] We have found that fault 2 either coalesces with or is repelled from fault 1 according to their initial configuration. There exists a critical value for the step over width across which the pattern is switched; for instance, under certain conditions, fault 2 coalesces with fault 1 if the step over is narrower than about 1/4 to 1/2 the length of fault 1, and mutual repulsion occurs otherwise. The orientation of fault bending can be explained in terms of the orientation of maximum shear due to fault 1 alone (see discussions in section 4.4).

[58] Fault 2 tended to bend more steeply when the rupture velocity was higher. This attests to the importance of considering dynamic effects when dealing with rapidly propagating rupture, an argument consistent with the implications of the studies by *Kame and Yamashita* [1999a, 1999b], *Poliakov et al.* [2002], and *Kame et al.* [2003].

[59] Our simulation results are able to explain why noncoplanar fault segments interconnected with bends at oblique angles are so often observed in natural fault systems; adjacent fault segments tend to coalesce and fault systems tend to lengthen as a result of dynamic interactions during rupture episodes.

[60] We have carried out our present modeling study under some simplifying assumptions, as our principal aim

lies in obtaining qualitative insights into the most basic characteristics of dynamic fault interactions. The effects of variable rupture velocity, different varieties of regional stress, and of more realistic friction laws such as slip weakening, should be considered for more quantitative studies in the future. We have reported, elsewhere, some preliminary results of modeling research in that direction [*Ando and Yamashita*, 2003b], and further results shall appear in subsequent papers.

Appendix A: Convolution Kernels for the Discrete BIEs

[61] Equation (1) is the discrete form of our basic BIEs which represent the shear traction T^{in} at any given spatial node i and time step n as a spatiotemporal convolution of the slip velocity profile history D^{jm} and static slip profile S^j with appropriate integration kernels (Green's functions). The shear traction at the ith spatial node and nth time step is represented by

$$T^{in} = \sum_j \left\{ N_1^{ij} N_2^{ij} \left[\sigma_{22}\left(X_1^{ij}, X_2^{ij}, t_n\right) - \sigma_{11}\left(X_1^{ij}, X_2^{ij}, t_n\right) \right] + \left[\left(N_2^{ij}\right)^2 - \left(N_1^{ij}\right)^2 \right] \sigma_{12}\left(X_1^{ij}, X_2^{ij}, t_n\right) \right\}, \tag{A1}$$

where σ_{lk} is the lk component of stress, due to the slip history on the jth element alone, measured in the local coordinate system (X_1, X_2) with the origin fixed at the jth node and the X_1 axis coinciding with the plane of the corresponding jth discrete element, (X_1^{ij}, X_2^{ij}) the location of the ith node, and (N_1^{ij}, N_2^{ij}) the normal vector to the ith element in this local coordinate system. In the global coordinate system (x_1, x_2), the latter two can be written as

$$\begin{aligned} N_1^{ij} &= n1^i n_2^j - n_2^i n_1^j \\ N_2^{ij} &= n_1^i n_1^j + n_2^i n_2^j \end{aligned} \tag{A2}$$

$$\begin{aligned} X_1^{ij} &= \left(x_1^i - x_1^j\right) n_2^j - \left(x_2^i - x_2^j\right) n_1^j \\ X_2^{ij} &= \left(x_1^i - x_1^j\right) n_1^j + \left(x_2^i - x_2^j\right) n_2^j, \end{aligned} \tag{A3}$$

where (x_1^j, x_2^j) is the location of the ith node and (n_1^i, n_2^i) is the normal vector to the corresponding ith element.

[62] In analogy to equation (1), the stress component σ_{lk} at the ith spatial node and nth time step, that is due to the dynamic slip velocity history D^{jm} and static slip S_j on the jth element alone, can be written, in the above mentioned local coordinate system centered at the jth node, in the form of a convolution:

$$\sigma_{lk}\left(X_1^{ij}, X_2^{ij}, t_n\right) = -\frac{\mu}{2\beta} \sum_{m \le n} D^{jm} K_{\mathrm{dyn};\sigma_{lk}}^{i,j,n,m} + \frac{\mu}{\pi}\left(1 - p^2\right) S^j K_{\mathrm{stat};\sigma_{lk}}^{i,j}. \tag{A4}$$

If we assume a piecewise constant slip velocity within the jmth spatiotemporal discrete element that has a size of Δs in space and Δt in time, the dynamic convolution kernels are expressed as [*Tada and Madariaga*, 2001]

$$\begin{aligned} K_{\mathrm{dyn};\sigma_{pq}}^{i,j,n,m} &= K_{\mathrm{dyn};\sigma_{pq}}\left(X_1^{ij}, X_2^{ij}, t_n, t_m\right) \\ &\equiv I_{\mathrm{dyn};\sigma_{pq}}\left(X_1^{ij} + \Delta s/2, X_2^{ij}, t_n - t_m + e_t \Delta t\right) \\ &- I_{\mathrm{dyn};\sigma_{pq}}\left(X_1^{ij} - \Delta s/2, X_2^{ij}, t_n - t_m + e_t \Delta t\right) \\ &- I_{\mathrm{dyn};\sigma_{pq}}\left[X_1^{ij} + \Delta s/2, X_2^{ij}, t_n - t_m - (1 - e_t)\Delta t\right] \\ &+ I_{\mathrm{dyn};\sigma_{pq}}\left[X_1^{ij} - \Delta s/2, X_2^{ij}, t_n - t_m - (1 - e_t)\Delta t\right], \end{aligned}$$

$$\begin{aligned} I_{\mathrm{dyn};\sigma_{11}}(x_1, x_2, t) = &-\frac{1}{\pi} H\left(t - \frac{r}{\alpha}\right) \frac{2x_2}{r} \\ &\cdot p \left\{ \frac{2\left(3x_1^2 - x_2^2\right)}{3r^2} p^2 \left[(\alpha t/r)^2 - 1 \right]^{3/2} \right. \\ &\left. + \left(1 - \frac{2x_2^2}{r^2} p^2\right) \sqrt{(\alpha t/r)^2 - 1} \right\} + \frac{1}{\pi} H\left(t - \frac{r}{\beta}\right) \\ &\cdot \frac{2x_2}{r} \left\{ \frac{2\left(3x_1^2 - x_2^2\right)}{3r^2} \left[(\beta t/r)^2 - 1 \right]^{3/2} + \left(1 - \frac{2x_2^2}{r^2}\right) \right. \\ &\left. \cdot \sqrt{(\beta t/r)^2 - 1} \right\}, \end{aligned} \tag{A6}$$

$$\begin{aligned} I_{\mathrm{dyn};\sigma_{22}}(x_1, x_2, t) = &\frac{1}{\pi} H\left(t - \frac{r}{\alpha}\right) \frac{2x_2}{r} \\ &\cdot p \left\{ \frac{2\left(3x_1^2 - x_2^2\right)}{3r^2} p^2 \left[(\alpha t/r)^2 - 1 \right]^{3/2} \right. \\ &\left. + \left(\frac{2x_1^2}{r^2} p^2 - 1\right) \sqrt{(\alpha t/r)^2 - 1} \right\} - \frac{1}{\pi} H\left(t - \frac{r}{\beta}\right) \\ &\cdot \frac{2x_2}{r} \left\{ \frac{2\left(3x_1^2 - x_2^2\right)}{3r^2} \left[(\beta t/r)^2 - 1 \right]^{3/2} + \left(\frac{2x_1^2}{r^2} - 1\right) \right. \\ &\left. \cdot \sqrt{(\beta t/r)^2 - 1} \right\}, \end{aligned} \tag{A7}$$

$$\begin{aligned} I_{\mathrm{dyn};\sigma_{12}}(x_1, x_2, t) = &H(x_1) H\left(t - \frac{|x_2|}{\beta}\right) - \frac{1}{\pi} \mathrm{sgn}(x_1) H\left(t - \frac{r}{\alpha}\right) \frac{2|x_1|}{r} \\ &\cdot p \left\{ \frac{2\left(3x_2^2 - x_1^2\right)}{3r^2} p^2 \left[(\alpha t/r)^2 - 1 \right]^{3/2} \right. \\ &\left. + \frac{2x_2^2}{r^2} p^2 \sqrt{(\alpha t/r)^2 - 1} \right\} + \frac{1}{\pi} \mathrm{sgn}(x_1) H\left(t - \frac{r}{\beta}\right) \\ &\cdot \left[\frac{2|x_1|}{r} \left\{ \frac{2\left(3x_2^2 - x_1^2\right)}{3r^2} \left[(\beta t/r)^2 - 1 \right]^{3/2} + \frac{2x_2^2}{r^2} \right. \right. \\ &\left. \left. \cdot \sqrt{(\beta t/r)^2 - 1} \right\} - \mathrm{Arc}\cos \frac{|x_1|}{\sqrt{(\beta t)^2 - x_2^2}} \right], \end{aligned} \tag{A8}$$

$$r = \sqrt{x_1^2 + x_2^2}, \tag{A9}$$

where e_t is a parameter of time collocation such that the nth time step t_n represents a time interval starting at $t_n - e_t \Delta t$ and ending at $t_n + (1 - e_t)\Delta t$; we take parameters $\alpha \Delta s/\Delta t = 0.5$ and $e_t = 1$ in the present study.

[63] Likewise, the convolution kernels representing the stress response to piecewise constant static slip on the jth element are given by

$$K^{i,j}_{\mathrm{stat};\sigma_{pq}} = K_{\mathrm{stat};\sigma_{pq}}\left(X_1^{ij}, X_2^{ij}\right) \equiv I_{\mathrm{stat};\sigma_{pq}}\left(X_1^{ij} + \Delta s/2, X_2^{ij}\right) - I_{\mathrm{stat};\sigma_{pq}}\left(X_1^{ij} - \Delta s/2, X_2^{ij}\right), \tag{A10}$$

$$I_{\mathrm{stat};\sigma_{11}}(x_1, x_2) = \frac{x_2}{r^2}\left(1 + 2\frac{x_1^2}{r^2}\right), \tag{A11}$$

$$I_{\mathrm{stat};\sigma_{22}}(x_1, x_2) = \frac{x_2}{r^2}\left(1 - 2\frac{x_1^2}{r^2}\right), \tag{A12}$$

$$I_{\mathrm{stat};\sigma_{12}}(x_1, x_2) = \frac{x_1}{r^2}\left(1 - 2\frac{x_1^2}{r^2}\right). \tag{A13}$$

Appendix B: Analytic Solutions for the Elastic Field Around an Isolated Fault

[64] According to *Pollard and Segall* [1987], the analytic solution for the static stress perturbation due to an isolated planar fault of half length L with a homogeneous shear stress drop $\Delta\sigma$ is given by

$$\frac{1}{2}(\sigma_{11} - \sigma_{22})/\Delta\sigma = \frac{r}{R}\sin(\psi - \Psi) - \frac{L^2 r}{R^3}\sin\psi\cos 3\Psi, \tag{B1}$$

$$\frac{1}{2}(\sigma_{11} + \sigma_{22})/\Delta\sigma = \frac{r}{R}\sin(\psi - \Psi), \tag{B2}$$

$$\frac{\sigma_{12}}{\Delta\sigma} = \frac{r}{R}\cos(\psi - \Psi) - 1 - \frac{L^2 r}{R^3}\sin\psi\sin 3\Psi, \tag{B3}$$

$$\sigma_{31}/\Delta\sigma = rR^{-1}\sin(\psi - \Psi), \tag{B4}$$

$$\sigma_{32}/\Delta\sigma = rR^{-1}\cos(\psi - \Psi) - 1, \tag{B5}$$

$$R = \sqrt{r_1 r_2}, \tag{B6}$$

$$\Psi = \frac{\psi_1 + \psi_2}{2} \tag{B7}$$

(see Figure B1 for the definition of r, r_1, r_2, Ψ, Ψ_1 and Ψ_2).

[65] The analytic solution for the dynamic stress perturbation due to a self-similar fault with a homogeneous shear stress drop $\Delta\sigma$ that is nucleated at the origin of coordinates at time $t = 0$ and propagated bilaterally along the x_1 axis at a constant rupture velocity v_r is given by [*Kostrov*, 1964; *Kikuchi*, 1976; *Tada*, 1995]

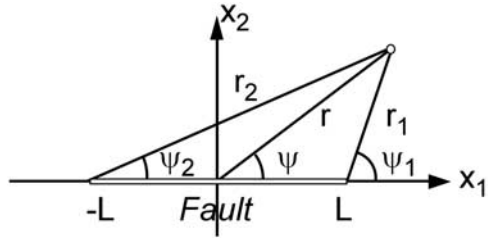

Figure B1. Definition of parameters appearing in equations (B1) to (B7).

$$\frac{1}{2}(\sigma_{11} - \sigma_{22})/\Delta\sigma = \frac{1}{P_{II}(v_r)}\mathrm{Im}\left[2\left(\frac{\beta^2}{\alpha^2} - \frac{2\beta^2}{v_r^2}\right)\frac{1}{v_r\sqrt{v_r^{-2} - \theta_\alpha^2}} - 2\left(1 - \frac{2\beta^2}{v_r^2}\right)\frac{1}{v_r\sqrt{v_r^{-2} - \theta_\beta^2}} + \frac{4\beta^2}{v_r^2}\left(\sqrt{v_r^{-2} - \theta_\beta^2} - \sqrt{v_r^{-2} - \theta_\alpha^2}\right)\right], \tag{B8}$$

$$\frac{1}{2}(\sigma_{11} + \sigma_{22})/\Delta\sigma = -\frac{1}{P_{II}(v_r)}2\left(1 - \frac{\beta^2}{\alpha^2}\right)\mathrm{Im}\left(\frac{1}{v_r\sqrt{v_r^{-2} - \theta_\alpha^2}}\right), \tag{B9}$$

$$\sigma_{12}/\Delta\sigma = -\frac{1}{P_{II}(v_r)}\frac{4\beta^2}{v_r}\mathrm{Im}\left[\int_0^{\theta_\alpha}\theta^2\left(\alpha^{-2} - \theta^2\right)^{1/2}\left(v_r^{-2} - \theta^2\right)^{-3/2}d\theta + \int_0^{\theta_\beta}\left(\frac{1}{2}\beta^{-2} - \theta^2\right)^2\left(\beta^{-2} - \theta^2\right)^{-1/2}\left(v_r^{-2} - \theta^2\right)^{-3/2}d\theta\right], \tag{B10}$$

$$\sigma_{31}/\Delta\sigma = -\frac{1}{P_{III}(v_r)}\mathrm{Im}\left(\frac{1}{v_r\sqrt{v_r^{-2} - \theta_\beta^2}}\right), \tag{B11}$$

$$\sigma_{32}/\Delta\sigma = -\frac{1}{P_{III}(v_r)}\frac{1}{v_r}\mathrm{Im}\left[\int_0^{\theta_\beta}\left(\beta^{-2} - \theta^2\right)^{1/2}\left(v_r^{-2} - \theta^2\right)^{-3/2}d\theta\right], \tag{B12}$$

$$\theta_c = \begin{cases} (t/r)\cos\phi + i\sqrt{(t/r)^2 - c^{-2}}\sin\phi & (r < ct) \\ (t/r)\cos\phi - \sqrt{c^{-2} - (t/r)^2}\sin\phi & (r \geq ct) \end{cases} \quad (c = \alpha, \beta), \tag{B13}$$

$$x_1 = r\cos\phi$$
$$x_2 = r\sin\phi, \tag{B14}$$

where the normalization factors $P_{II}(v_r)$ and $P_{III}(v_r)$ are

$$P_{II}(v_r) = \frac{v_r^2}{\beta^2 - v_r^2}\left(K_\beta - E_\beta\right) + \frac{8\beta^2}{v_r^2}\left(E_\alpha - E_\beta\right) + 4\left(K_\beta - \frac{\beta^2}{\alpha^2}K_\alpha\right) \tag{B15}$$

$$P_{III}(v_r) = E_\beta \tag{B16}$$

with

$$K_c \equiv K(\pi/2, k_c), E_c \equiv E(\pi/2, k_c), k_c \equiv \sqrt{1 - (v_r/c)^2} \tag{B17}$$

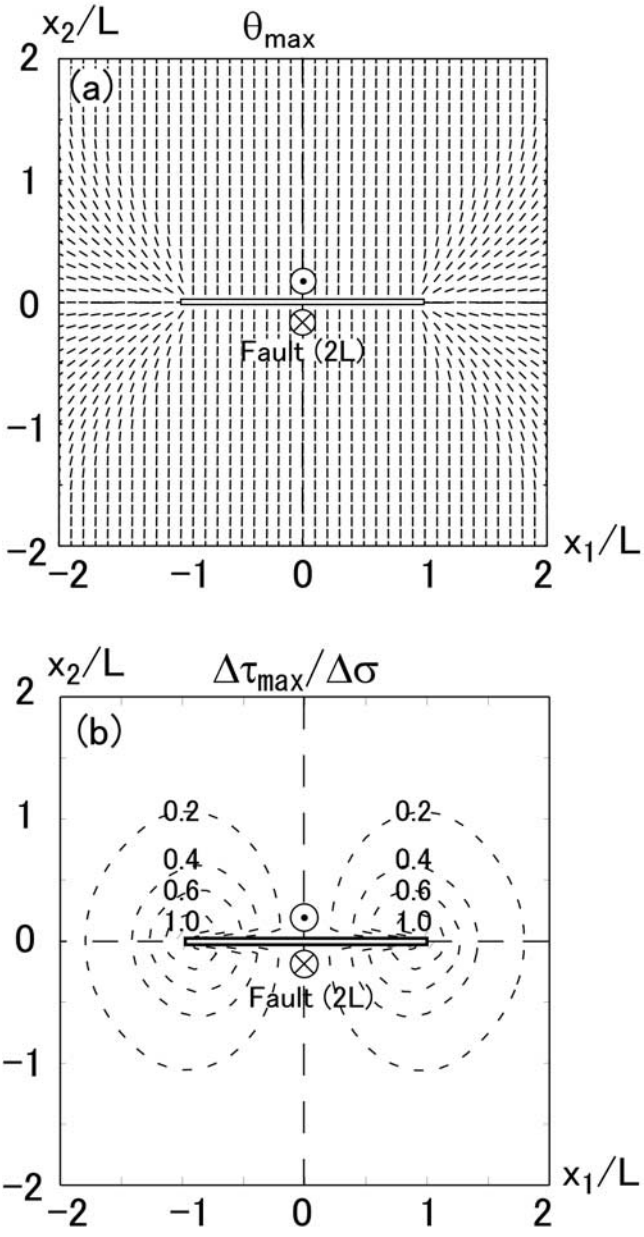

Figure C1. Spatial distribution of the (a) orientation and (b) magnitude of the maximum static shear traction $\Delta\tau_{max}$ around an isolated fault in antiplane shear.

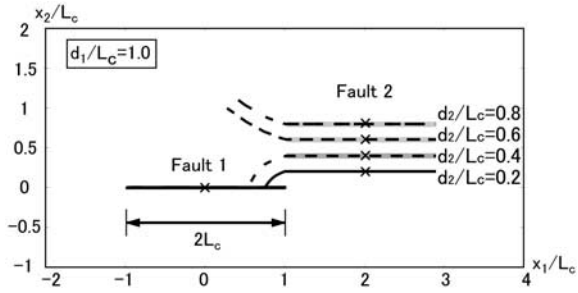

Figure D1. Final fault geometry for model D, with the spatiotemporal grid intervals twice refined with respect to the characteristic length of the fault system.

being complete elliptic integrals of the first and second kinds, respectively.

Appendix C: Dynamic Evolution of Fault Geometry in Antiplane Shear

[66] In the present study, we have simulated the dynamic evolution of the geometry of a system of two noncoplanar faults in in-plane shear (mode II) and have found the occurrence of coalescence or mutual repulsion depending on the initial configuration. What happens, then, to a system of two noncoplanar faults in antiplane shear (mode III)?

[67] Figure C1a shows the distribution of the orientation θ_{max} of the maximum static shear traction around an isolated fault in antiplane shear. We observe, for example, that $0^\circ < \theta_{max} < 90^\circ$ holds over the entire area of the first quadrant, and there is nothing like the boundaries E and L which we have defined in the in-plane shear case. The same sort of argument we developed in section 4.4 leads us to expect that coalescence is likely to happen between two noncoplanar faults as long as the initial overlap is smaller than half the length of the individual faults. This was in fact the case when we conducted numerical simulations; mutual repulsion never happened under such conditions.

Appendix D: Effects of Discretization

[68] To test the sensitivity of the simulation results on the level of discretization, we conducted another set of numerical tests for model S, with the initial geometry identical to the case $d_2 = 0.2L_c$ in Figure 10b, with the spatiotemporal grid intervals twice refined so that $2L_c = 44\Delta s$ (Figure D1). The trajectory of fault 2 in the step over region became less rugged than in Figure 10b as a result of the more accurate evaluation of the local stress field in the close vicinity of the fault tip; as we have said in section 2.2, we evaluate the hoop shear at the midpoint of the fault element to be broken next, and the distance of that point from the tip of the fault has been halved relative to the characteristic length L_c of the fault system. Nonetheless, the pattern of dependence of the final geometry, coalescence or repulsion, on the step over width d_2 remained the same as in Figure 10b.

[69] **Acknowledgments.** We appreciate reviews by David D. Oglesby, Eiichi Fukuyama, and an anonymous Associate Editor that contributed to

a significant improvement on our original manuscript. We are also grateful to Nobuki Kame for a number of constructive discussions. This work was partially supported by the DaiDaiToku Project, MEXT, Japan.

References

Ando, R., and T. Yamashita (2003a), Dynamic interactions between fault segments and the formation of fault system (in Japanese with English abstract), *J. Seismol. Soc. Jpn.*, *56*, 1–9.

Ando, R., and T. Yamashita (2003b), Fault interactions as origin of fault bending and complexity of dynamic rupture process, paper presented at the IUGG XXIII General Assembly, Sapporo, Japan.

Aochi, H., and E. Fukuyama (2002), Three-dimensional nonplanar simulation of the 1992 Landers earthquake, *J. Geophys. Res.*, *107*(B2), 2035, doi:10.1029/2000JB000061.

Aochi, H., E. Fukuyama, and M. Matsu'ura (2000), Spontaneous rupture propagation on a non-planar fault in 3-D elastic medium, *Pure Appl. Geophys.*, *157*, 2003–2027.

Bilham, R., and P. Williams (1985), Sawtooth segmentation and deformation processes on the southern San Andreas fault, California, *Geophys. Res. Lett.*, *12*, 557–560.

Cochard, A., and R. Madariaga (1994), Dynamic faulting under rate-dependent friction, *Pure Appl. Geophys.*, *142*, 419–445.

Du, Y., and A. Aydin (1993), The maximum distortional strain energy density criterion for shear fracture propagation with applications to the growth paths of en échelon faults, *Geophys. Res. Lett.*, *20*, 1091–1094.

Du, Y., and A. Aydin (1995), Shear fracture patterns and connectivity at geometric complexities along strike-slip faults, *J. Geophys. Res.*, *100*, 18,093–18,102.

Freund, L. B. (1990), *Dynamic Fracture Mechanics*, Cambridge Univ. Press, New York.

Granier, T. (1985), Origin, damping, and pattern of development of faults in granite, *Tectonics*, *4*, 721–737.

Harris, R. A., and S. M. Day (1993), Dynamics of fault interaction: Parallel strike-slip faults, *J. Geophys. Res.*, *98*, 4461–4472.

Harris, R. A., and S. M. Day (1999), Dynamic 3D simulations of earthquakes on en echelon faults, *Geophys. Res. Lett.*, *26*, 2089–2092.

Harris, R. A., R. J. Archuleta, and S. M. Day (1991), Fault steps and the dynamic rupture process: 2-D numerical simulations of a spontaneously propagating shear fracture, *Geophys. Res. Lett.*, *18*, 893–896.

Kame, N., and T. Yamashita (1999a), A new light on arresting mechanism of dynamic earthquake faulting, *Geophys. Res. Lett.*, *26*, 1997–2000.

Kame, N., and T. Yamashita (1999b), Simulation of the spontaneous growth of a dynamic crack without constraints on the crack tip path, *Geophys. J. Int.*, *139*, 345–358.

Kame, N., and T. Yamashita (2003), Dynamic branching, arresting of rupture and the seismic wave radiation in self-chosen crack path modelling, *Geophys. J. Int.*, *155*, 1042–1050.

Kame, N., J. R. Rice, and R. Dmowska (2003), Effects of pre-stress state and rupture velocity on dynamic fault branching, *J. Geophys. Res.*, *108*(B5), 2265, doi:10.1029/2002JB002189.

Kikuchi, M. (1976), Displacement velocity and stress fields caused by a two-dimensional self-similar crack (in Japanese with English abstract), *J. Seismol. Soc. Jpn.*, *29*, 277–285.

King, G., and J. Nábělek (1985), Role of fault bends in the initiation and termination of earthquake rupture, *Science*, *228*, 984–987.

Koller, M. G., M. Bonnet, and R. Madariaga (1992), Modelling of dynamical crack propagation using time-domain boundary integral equations, *Wave Motion*, *16*, 339–366.

Kostrov, B. V. (1964), Self-similar problems of propagation of shear cracks, *J. Appl. Math. Mech.*, Engl. Transl., *28*, 1077–1087.

Lei, X., K. Kusunose, M. V. M. S. Rao, O. Nishizawa, and T. Satoh (2000), Quasi-static fault growth and cracking in homogeneous brittle rock under triaxial compression using acoustic emission monitoring, *J. Geophys. Res.*, *105*, 6127–6139.

Lockner, D. A., J. D. Byerlee, V. Kuksenko, A. Ponomarev, and A. Sidorin (1992), Observations of quasistatic fault growth from acoustic emissions, in *Fault Mechanics and Transport Properties of Rocks*, *Int. Geophys. Ser.*, vol. 51, edited by B. Evans and T. F. Wong, pp. 3–31, Academic, San Diego, Calif.

Moore, D. E., and D. A. Lockner (1995), The role of microcracking in shear-fracture propagation in granite, *J. Struct. Geol.*, *17*, 95–114.

Olson, J. E., and D. D. Pollard (1991), The initiation and growth of en échelon veins, *J. Struct. Geol.*, *13*, 595–608.

Poliakov, A. N. B., R. Dmowska, and J. R. Rice (2002), Dynamic shear rupture interactions with fault bends and off-axis secondary faulting, *J. Geophys. Res.*, *107*(B11), 2295, doi:10.1029/2001JB000572.

Pollard, D. D., and P. Segall (1987), Theoretical displacements and stresses near fractures in rock: With applications to faults, joints, veins, dikes, and solution surfaces, in *Fracture Mechanics of Rock*, edited by B. K. Atkinson, pp. 277–349, Academic, San Diego, Calif.

Reches, Z., and D. A. Lockner (1994), Nucleation and growth of faults in brittle rocks, *J. Geophys. Res.*, *99*, 18,159–18,173.

Renshaw, C. E., and D. D. Pollard (1994), Are large differential stresses required for straight fracture propagation paths?, *J. Struct. Geol.*, *16*, 817–822.

Scholz, C. H. (2002), *The Mechanics of Earthquakes and Faulting*, 2nd ed., Cambridge Univ. Press, New York.

Seelig, T., and D. Gross (1999), On the interaction and branching of fast running cracks—A numerical investigation, *J. Mech. Phys. Solids*, *47*, 935–952.

Segall, P., and D. D. Pollard (1983), Nucleation and growth of strike-slip faults in granite, *J. Geophys. Res.*, *88*, 555–568.

Segall, P., and C. Simpson (1986), Nucleation of ductile shear zones on dilatant fractures, *Geology*, *14*, 56–59.

Sibson, R. H. (1986a), Brecciation process in fault zones: Inferences from earthquake rupturing, *Pure Appl. Geophys.*, *124*, 159–175.

Sibson, R. H. (1986b), Rupture interaction with fault jogs, in *Earthquake Source Mechanics*, *Geophys. Monogr. Ser.*, vol. 37, edited by S. Das, J. Boatwright, and C. H. Scholz, pp. 157–167, AGU, Washington, D. C.

Sieh, K., et al. (1993), Near-field investigations of the Landers earthquake sequence, April to July 1992, *Science*, *260*, 171–176.

Sowers, J. M., J. R. Unruh, W. R. Lettis, and T. D. Rubin (1994), Relationship of the Kickapoo fault to the Johnson Valley and Homestead Valley faults, San Bernardino County, California, *Bull. Seismol. Soc. Am.*, *84*, 528–536.

Tada, T. (1995), Boundary integral equations for the time-domain and time-independent analyses of 2D non-planar cracks, D.Sc. thesis, Univ. of Tokyo, Tokyo.

Tada, T., and R. Madariaga (2001), Dynamic modelling of the flat 2-D crack by a semi-analytic BIEM scheme, *Int. J. Numer. Methods Eng.*, *50*, 227–251.

Tada, T., and T. Yamashita (1997), Non-hypersingular boundary integral equations for two-dimensional non-planar crack analysis, *Geophys. J. Int.*, *130*, 269–282.

Tchalenko, J. S., and M. Berberian (1975), Dasht-e-Bayaz fault, Iran: Earthquake and earlier related structures in bed rock, *Geol. Soc. Am. Bull.*, *86*, 703–709.

Wald, D. J., and T. H. Heaton (1994), Spatial and temporal distribution of slip for the 1992 Landers, California, earthquake, *Bull. Seismol. Soc. Am.*, *84*, 668–691.

Yamashita, T., and E. Fukuyama (1996), Apparent critical slip displacement caused by the existence of a fault zone, *Geophys. J. Int.*, *125*, 459–472.

R. Ando and T. Yamashita, Earthquake Research Institute, University of Tokyo, 1-1-1 Yayoi, Bunkyo-ku, Tokyo 113-0032, Japan. (ando@eri.u-tokyo.ac.jp; tyama@eri.u-tokyo.ac.jp)

T. Tada, Department of Architecture, Faculty of Engineering, Tokyo University of Science, Kagurazaka 1-3, Shinjuku-ku, Tokyo 162-8601, Japan. (kogutek@rs.kagu.tus.ac.jp)